Orientation dependence of harmonic emission from vibrating HeH^{2+} versus HeT^{2+}: Effects of a permanent dipole

Y. P. Li,[1] S. J. Yu,[1] W. Y. Li,[2,*] and Y. J. Chen[1,†]

[1]*College of Physics and Information Technology, Shaan'xi Normal University, Xi'an 710119, China*

[2]*School of Mathematics and Science, Hebei GEO University, Shijiazhuang 050031, China*

(Received 18 April 2017; published 14 June 2017)

We study high-order harmonic generation (HHG) from the oriented asymmetric molecule HeH^{2+} and its isotopic variant HeT^{2+} in strong few-cycle laser pulses, by numerically solving the non-Born-Oppenheimer time-dependent Schrödinger equation. Our simulations show that the influence of nuclear motion on HHG of the asymmetric system is dependent on the molecular orientation and the laser parameters. At relatively weak laser intensities, the HHG yields of HeH^{2+} are higher than those of HeT^{2+} for the parallel orientation and the situation reverses for the perpendicular orientation. However, at high laser intensities, they become comparable for the parallel case. With a developed simple HHG model that considers the influences of nuclear motion on all of the ionization, propagation, and recombination processes of HHG, we show the permanent dipole of the system plays an important role in these phenomena. Our results shed light on the complex dynamics of the asymmetric system in strong laser fields.

DOI: 10.1103/PhysRevA.95.063412

I. INTRODUCTION

High-order harmonics generation (HHG) from atoms and molecules [1] and solids [2] has been a popular subject in both theoretical and experimental studies of strong-laser-matter interactions in recent years. It has important applications in attosecond physics [3] such as producing attosecond pulses [4–6] and attosecond probing of molecular structure [7–10] and electron dynamics [11–13]. The HHG is also capable of probing the nuclear motion [14,15] and tracing a chemical reaction [16] in the ultrafast time scale. The HHG process is well described by a three-step model [17,18]: tunneling ionization of the bound electron from the laser-dressed potential; propagation of the freed electron in strong laser fields; and recombination of the rescattering electron with its parent ion with the emission of a high-energy photon.

In comparison with atoms, molecules with more degrees of freedom show some new physical phenomena in the HHG process, such as charge-resonance effects [19–23], orientation effects [24–26], two-center-interference effects [27–30], polarization [31–36], and so on. The theoretical study of molecular HHG is usually based on the Born-Oppenheimer (BO) approximation, where the motion of the nuclei is neglected. This approximation is generally reasonable since the motion of the electron is much faster than the nuclei. The BO approximation has been widely used in the study of HHG from heavier molecules such as O_2 and N_2 [26] and CO_2 [28,29]. However, for lighter molecules such as H_2 [14] and H_2^+ [15,37], it has been shown that the motion of the nuclei plays an important role in the HHG. Due to the influence of nuclear motion, the HHG yields are lower for H_2 than T_2 [14], and somewhat higher for H_2^+ than D_2^+ [15]. In addition, to study the dissociation-related processes of molecules in strong laser fields such as the stretching of Br_2 [16] in photodissociation, it is also necessary to consider the nuclear motion.

For asymmetric molecules with a large permanent dipole, such as NO [38], N_2O [39], HCl [40], HeH^{2+} [41–45], CO [46–54], and OCS [55], the situation is more complex. It has been shown that the permanent dipole of the asymmetric molecule leads to asymmetric ionization [41], the large Stark effect [47], and multichannel emission of harmonics [42,43]. In particular, as the nuclear motion is considered, there are six possible recombination channels, which can be identified in the HHG process of HeH^{2+} [56]. The permanent dipole also induces the quick nuclear motion for the asymmetric system HeH^+ [57] in comparison with the symmetric case of H_2.

The effect of the permanent dipole is dependent on the molecular orientation. One can expect that the orientation effect will importantly influence the electron-nuclei coupled dynamics of asymmetric molecules. As the orientation effect related to molecular HHG has been widely studied in the fixed-nuclei case, it is less studied in the vibrating case, especially for the vibrating asymmetric system. To understand the complex dynamics of asymmetric molecules in strong laser fields, a detailed study in the HHG from oriented asymmetric molecules beyond the BO approximation is desired.

In this paper, through numerical solution of the non-BO time-dependent Schrödinger equation (TDSE) for HeH^{2+} with two-dimensional electron dynamics and one-dimensional nuclear dynamics, we explore the influence of molecular orientation on the HHG of vibrating HeH^{2+}, along with comparing it to its isotopic variant HeT^{2+} and changing the laser parameters such as the laser intensity and the laser wavelength. When the laser polarization is parallel to the molecular axis (the parallel orientation), the calculated HHG yields of HeH^{2+} are almost one order of magnitude higher than HeT^{2+}. This situation reverses for the perpendicular orientation. At high laser intensities, the HHG yields of these two molecules become comparable for the parallel case. Our analyses reveal that the effect of the permanent dipole associated with the molecular orientation and the laser parameters plays an important role in these phenomena. With

*liweiyanhb@126.com

†chenyjhb@gmail.com

the development of a simple HHG model that considers the nuclear vibration, the roles of nuclear motion in all of the ionization, propagation and recombination processes of HHG is addressed in detail.

II. THEORETICAL DESCRIPTIONS

A. Numerical procedure

1. TDSE simulations

We assume that the laser field is along the x axis, the molecular axis is located in the xy plane and the center of mass of the molecular system is located at the origin of the coordinate system o. The TDSE of the asymmetric system studied here has the following form (in atomic units of $\hbar = e = m_e = 1$)

$$i\frac{\partial\psi(R,\boldsymbol{r},t)}{\partial t} = [H_0 + V_I(t)]\psi(R,\boldsymbol{r},t). \tag{1}$$

Here $H_0 = T_N + T_e + V_{\rm eff}(R,\mathbf{r})$ is the field-free Hamiltonian with

$$T_N = -\frac{1}{2\mu_N}\frac{\partial^2}{\partial R^2}, \tag{2}$$

$$T_e = -\frac{1}{2\mu_e}\frac{\partial^2}{\partial \mathbf{r}^2} = -\frac{1}{2\mu_e}\left[\frac{\partial^2}{\partial x^2} + \frac{\partial^2}{\partial y^2}\right], \tag{3}$$

$$V_{\rm eff}(R,\mathbf{r}) = \frac{Z_{\rm He}Z_H}{R} - \frac{Z_{\rm He}e^{-\rho(R)r_{\rm He}^2}}{\sqrt{r_{\rm He}^2+\varepsilon}} - \frac{Z_H e^{-\rho(R)r_H^2}}{\sqrt{r_H^2+\varepsilon}}. \tag{4}$$

Here $\mu_N = M_{\rm He}M_H/(M_{\rm He}+M_H)$ is the nuclear reduced mass, and $\mu_e = (M_{\rm He}+M_H)/(M_{\rm He}+M_H+1)$ is the electronic reduced mass. $M_{\rm He}$ and M_H are masses of He and H nuclei. $Z_{\rm He} = 2$ and $Z_H = 1$ are the charges for the He and H centers. R is the internuclear separation. $r_{\rm He}^2 = (\boldsymbol{r} - \boldsymbol{R}_{\rm He})^2 = (x - R_{\rm He}\cos\theta)^2 + (y - R_{\rm He}\sin\theta)^2$ and $r_H^2 = (\boldsymbol{r} - \boldsymbol{R}_H)^2 = (x + R_H\cos\theta)^2 + (y + R_H\sin\theta)^2$. $\mathbf{r}$ is the position of the electron to the origin, and θ is the angle between the molecular axis and the laser polarization. $\boldsymbol{R}_{\rm He}$ and $\boldsymbol{R}_H$ are the positions of the He and H nuclei with $R_{\rm He} = M_H R/(M_H+M_{\rm He})$ and $R_H = M_{\rm He}R/(M_H+M_{\rm He})$. $\varepsilon = 0.16$ is the softening parameter. $\rho(R)$ is the screening parameter, which is adjusted such that the resulting 2σ BO potential of the model molecule matches the real 2σ BO potential of HeH^{2+} calculated with the approach introduced in Ref. [41]. In this case with $\varepsilon = 0.16$, the resulting 1σ BO potential of the model molecule is also very near to the real 1σ BO potential of HeH^{2+}. The HeH^{2+} system has a stable 2σ state with the equilibrium distance of $R_2 = 3.9$a.u. and the ionization potential of $I_p = 0.53$a.u.. This state is chosen as the initial state in our TDSE simulations.

In Eq. (1), the term $V_I(t)$ describes the interaction of the HeH^{2+} system and the laser field. The laser field used here has the form of $\boldsymbol{\xi}(t) = \vec{\mathbf{e}}_x\xi(t) = \vec{\mathbf{e}}_x f(t)E_0\sin\omega_0 t$ with the amplitude E_0, the frequency ω_0, and the envelope function $f(t)$. The symbol $\vec{\mathbf{e}}_x$ denotes the unit vector along the laser polarization. In the dipole approximation and the length gauge, the term $V_I(t)$ in our calculations has the following form [57,58]

$$V_I(t) = V_I^e(\mathbf{r},t) + V_I^n(R,t) = x\xi(t) - \gamma R\xi(t)\cos\theta, \tag{5}$$

with $\gamma = (Z_{\rm He}M_H - Z_H M_{\rm He})/(M_{\rm He}+M_H)$. Considering the respective mass of He (including two protons and two neutrons), H (one proton) and T (one proton and two neutrons), the value of γ is $-2/5$ for HeH^{2+} and it is $2/7$ for HeT^{2+}. The first term $V_I^e(\mathbf{r},t) = x\xi(t)$ in Eq. (5) describes the laser-electron interaction. The second term $V_I^n(R,t) = -\gamma R\xi(t)\cos\theta$ describes the laser-nuclei interaction. Similar to the case of HeH^+ in Ref. [57], our extended simulations show that this term $V_I^n(R,t)$ also plays a small role in the HHG of HeH^{2+}.

In our simulations, we use a seven-cycle laser pulse, which is linearly turned on and off for two optical cycles, and then kept at a constant intensity for three additional cycles. The TDSE of Eq. (1) is solved numerically using the spectral method [59]. A grid size of $Lx \times Ly = 409.6 \times 51.2$a.u with the steps of $\Delta x = \Delta y = 0.4$a.u. for the electron and a range of $R = 2.5,\ldots,15.3$a.u. with the step of $\Delta R = 0.1$a.u. for the internuclear distance have proven sufficient for converged HHG spectra. The time step used in our calculations is $\Delta t = 0.05$a.u.. In each time step, a $\cos^{1/8}$ mask function is used in the boundary of each dimension to absorb the continuum wave packet. The mask function along the x axis has the form of $F(x) = \cos^{1/8}[\pi(|x| - x_0)/(L_x - 2x_0)]$ for $|x| \geqslant x_0$ and $F(x) = 1$ for $|x| < x_0$. $x_0 = L_x/8$ is the absorbing boundary. The mask function $F(y)$ along the y axis is similar to $F(x)$. A similar absorbing procedure with the mask function $F(R)$ is also used for the upper boundary of R.

2. Electronic states and vibrational states

At the frame of BO approximation with R as a parameter, the wave function for the eigenstate of the field-free Hamiltonian H_0 of Eq. (1) can be written as $\chi_n^\upsilon(R)\phi_n(R,\mathbf{r})$ with $\upsilon = 0,1,2,\ldots$. Here, $\phi_n(R,\mathbf{r})$ is the electronic BO wave function corresponding to the nth eigenstate and $\chi_n^\upsilon(R)$ is the vibrational wave function associated with $\phi_n(R,\mathbf{r})$. The BO wave function $\phi_n(R,\mathbf{r})$ and the BO potential $V_n(R)$ associated with $\phi_n(R,\mathbf{r})$ can be obtained through imaginary-time propagation of the Hamiltonian

$$H_0^e(R,\mathbf{r}) = T_e + V_{\rm eff}(R,\mathbf{r}). \tag{6}$$

With diagonalizing the nuclear Hamiltonian

$$H_0^n(R) = T_N + V_n(R), \tag{7}$$

we can then obtain the vibrational eigenstates $\chi_n^\upsilon(R)$ and eigenenergy E_n^υ associated with $\phi_n(R,\mathbf{r})$. Here, E_n^υ is also the energy of the whole Hamiltonian H_0 of Eq. (1) including electronic and nuclear motions. Using the above approach, we evaluate the BO wave function $\chi_1^0(R)\phi_1(R,\mathbf{r})$ for the first excited state 2σ of the system with the eigenenergy E_1^0, which will be used as the initial state in our TDSE simulations. With tracing the time evolution of the BO eigenstates obtained using the above approach, one can also analyze the bound-state dynamics of the system, as shown in Fig. 4 and Fig. 5.

3. *Rescattering wave packet*

The rescattering wave packet $\psi_{re}(R,\mathbf{r},t)$ has been shown to include full dynamical information of the rescattering electron. It can be obtained numerically following the procedure introduced in Ref. [60]. That is

$$\psi_{re}(R,\mathbf{r},t) = f(r,r_c)\psi_c(R,\mathbf{r},t), \tag{8}$$

where

$$f(r,r_c) = 1 \ \ (r = |\mathbf{r}| < r_c),$$
$$f(r,r_c) = \exp[-(r-r_c)^2/\Delta^2] \ \ (r \geqslant r_c)$$

with $r_c = 10$a.u. and $\Delta = 2$. The rescattering wave packet evaluated here is not sensitive to the choice of the parameters r_c and Δ. The function $\psi_c(R,\mathbf{r},t)$ appearing in the above expression is the continuum wave packet, which can be obtained with excluding the components of the electronic BO bound states $\phi_n(R,\boldsymbol{r})$ from $\psi(R,\boldsymbol{r},t)$. That is, $\psi_c(R,\boldsymbol{r},t) = \psi(R,\boldsymbol{r},t) - \Sigma_n a_n(R,t)\phi_n(R,\boldsymbol{r})$ with $a_n(R,t) = \langle\phi_n(R,\boldsymbol{r})|\psi(R,\boldsymbol{r},t)\rangle$. In our simulations, only the lower bound states such as the first excited state $\phi_1(R,\boldsymbol{r})$ (the initial state) and the second excited state $\phi_2(R,\boldsymbol{r})$ have large amplitudes. So we have $\psi_c(R,\boldsymbol{r},t) \approx \psi(R,\boldsymbol{r},t) - a_1(R,t)\phi_1(R,\boldsymbol{r}) - a_2(R,t)\phi_2(R,\boldsymbol{r})$. With the rescattering wave packet obtained using the above approach, one can analyze the continuum-state dynamics of the system, as shown in Figs. 6–10.

4. *HHG spectrum*

Once the TDSE wave function $\psi(t) \equiv \psi(R,\boldsymbol{r},t)$ is obtained, the coherent part of the HHG spectrum parallel to the laser polarization can be evaluated using

$$F(\omega) = \int \langle\psi(t)|\vec{\mathbf{e}}_x \cdot \boldsymbol{\nabla}_{\boldsymbol{r}} V_{\rm eff}|\psi(t)\rangle e^{i\omega t}dt, \tag{9}$$

where ω is the harmonic frequency and $V_{\rm eff} \equiv V_{\rm eff}(R,\mathbf{r})$. The HHG spectra of HeH^{2+} and HeT^{2+} obtained with Eq. (9) are shown in Fig. 1.

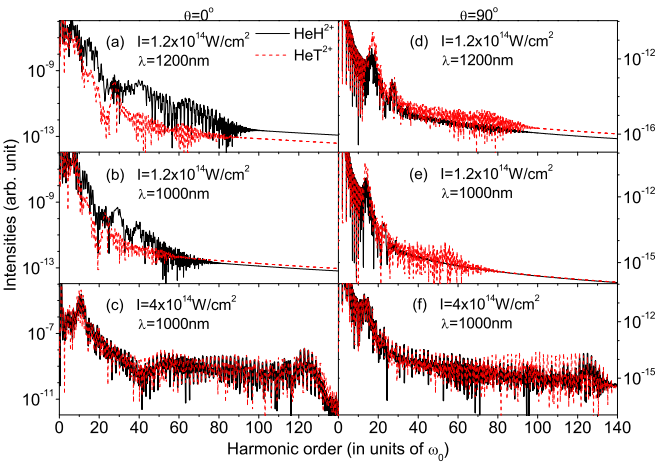

FIG. 1. Comparisons of HHG yields for HeH^{2+} (black solid) and HeT^{2+} (red dashed) at $\theta = 0^\circ$ (the left column) and $\theta = 90^\circ$ (right), obtained with different laser intensities and wavelengthes, as shown.

With considering the transition of the electron back to only the electronic 2σ BO state $\phi_1(R,\boldsymbol{r})$, Eq. (9) can be approximated as

$$F^1(\omega) \approx \int \langle\psi_1(t)|\vec{\mathbf{e}}_x \cdot \boldsymbol{\nabla}_{\boldsymbol{r}} V_{\rm eff}|\psi(t)\rangle e^{i\omega t}dt, \tag{10}$$

with $\psi_1(t) \equiv \psi_1(R,\mathbf{r},t) = a_1(R,t)\phi_1(R,\boldsymbol{r})$ and $a_1(R,t) = \langle\phi_1(R,\boldsymbol{r})|\psi(t)\rangle$. Considering the definition of the rescattering wave packet $\psi_{re}(t) \equiv \psi_{re}(R,\mathbf{r},t)$, the above expression can be further approximated as

$$F^{1,r}(\omega) \approx \int \langle\psi_1(t)|\vec{\mathbf{e}}_x \cdot \boldsymbol{\nabla}_{\boldsymbol{r}} V_{\rm eff}|\psi_{re}(t)\rangle e^{i\omega t}dt. \tag{11}$$

Our extended simulations show that for HeH^{2+} in ultrashort laser pulses, the spectra of $F^{1,r}(\omega)$ evaluated with the rescattering wave packet $\psi_{re}(t)$ and the bound wave packet $\psi_1(t)$ are comparable to the accurate ones of $F(\omega)$ with the full TDSE wave function $\psi(t)$. We therefore can explore the HHG mechanism of the vibrating system through analyzing the bound and rescattering wave packets $\psi_1(R,\mathbf{r},t)$ and $\psi_{re}(R,\mathbf{r},t)$, which are closely relevant to the HHG, as shown later.

B. Analytical description: A simple HHG model

Now, we explore the influence of the laser-induced nuclear motion on the HHG of asymmetric molecules. Let us return to the expression of $F^{1,r}(\omega)$ of Eq. (11).

With expanding $\psi_{re}(R,\mathbf{r},t)$ on the electronic BO continuum state $\phi_{\mathbf{p}}(R,\mathbf{r})$, we have $\psi_{re}(R,\mathbf{r},t) = \int c_{\mathbf{p}}(R,t)\phi_{\mathbf{p}}(R,\mathbf{r})d\mathbf{p}$. Considering $\psi_1(R,\mathbf{r},t) = a_1(R,t)\phi_1(R,\mathbf{r})$, we arrive at

$$F^{1,r}(\omega) \approx \iint a_{\mathbf{p}}(R)d(R,\mathbf{p})dRd\mathbf{p}, \tag{12}$$

with $d(R,\mathbf{p}) = \langle\phi_1(R,\mathbf{r})|\vec{\mathbf{e}}_x \cdot \boldsymbol{\nabla}_{\mathbf{r}} V_{\rm eff}|\phi_{\mathbf{p}}(R,\mathbf{r})\rangle$, and

$$a_{\mathbf{p}}(R) = \int a_1^*(R,t)c_{\mathbf{p}}(R,t)e^{i\omega t}dt. \tag{13}$$

Here, the term $d(R,\mathbf{p})$ is the dipole of the electron between the BO first-excited state $\phi_1(R,\mathbf{r})$ and the continuum state $\phi_{\mathbf{p}}(R,\mathbf{r})$. The dipole term is closely associated with the molecular structure and is the same for a molecule and its isotopic variant such as HeH^{2+} and HeT^{2+}. This amplitude $a_{\mathbf{p}}(R)$ reflects the overlap of the bound wave packet $\psi_1(R,\mathbf{r},t)$ and the rescattering wave packet $\psi_{re}(R,\mathbf{r},t)$, and differs for HeH^{2+} and HeT^{2+}. If we consider that the main contribution to the harmonic ω comes from the continuum electron with the energy $E_{\mathbf{p}} = \mathbf{p}^2/2$ agreeing with $\omega = E_{\mathbf{p}} + I_p$, we also have

$$F^{1,r}(\omega) \sim \int a_{\mathbf{p}(\omega)}(R)d[R,\mathbf{p}(w)]dR, \tag{14}$$

with $p(w) = \sqrt{2(\omega - I_p)}$. The above expression clearly shows the dependence of the HHG on the nuclear motion characterized by the amplitude $a_{\mathbf{p}(\omega)}(R)$. This amplitude is influenced by both the dynamics of the bound wave packet $\psi_1(R,\mathbf{r},t)$ and the continuum one $\psi_{re}(R,\mathbf{r},t)$. The dynamical evolution of $\psi_1(R,\mathbf{r},t)$ is different from that of $\psi_{re}(R,\mathbf{r},t)$.

As discussed in Ref. [57], the amplitude $a_1(R,t) = \sum_\upsilon a_1^\upsilon(t)\chi_1^\upsilon(R)$ of the bound wave packet is influenced by the effect of the permanent dipole. This influence can be understood with a two-level model. Under two-level

approximations, with expanding the wave function $\psi(R,\mathbf{r},t)$ on the two lowest vibrational states $|0\rangle = \chi_1^{v=0}(R)\phi_1(R,r)$ and $|1\rangle = \chi_1^{v=1}(R)\phi_1(R,r)$, we have $\psi(R,\mathbf{r},t) = a_1^0(t)|0\rangle + a_1^1(t)|1\rangle$. Then the Schrödinger equation can be written as

$$\begin{aligned} i\dot{a}_1^0(t) &= a_1^0(t)\big[E_1^0 + \boldsymbol{\xi}(t)\cdot\langle 0|\mathbf{r}|0\rangle\big] + a_1^1(t)[\boldsymbol{\xi}(t)\cdot\langle 0|\mathbf{r}|1\rangle]; \\ i\dot{a}_1^1(t) &= a_1^1(t)\big[E_1^1 + \boldsymbol{\xi}(t)\cdot\langle 1|\mathbf{r}|1\rangle\big] + a_1^0(t)[\boldsymbol{\xi}(t)\cdot\langle 1|\mathbf{r}|0\rangle]. \end{aligned} \tag{15}$$

Here, the dipole terms $\langle 0(1)|\mathbf{r}|0(1)\rangle$ and $\langle 0(1)|\mathbf{r}|1(0)\rangle$ are defined as $\langle m|\mathbf{r}|m\rangle = \int |\chi_1^m(R)|^2\mathbf{D}_p(R)dR, \langle m|\mathbf{r}|n\rangle = \int[\chi_1^m(R)]^*\chi_1^n(R)\mathbf{D}_p(R)dR$, respectively. E_1^0 and E_1^1 are the energy of these two states $|0\rangle$ and $|1\rangle$. In the above expressions, the term

$$\mathbf{D}_p(R) = \int |\phi_1(R,\mathbf{r})|^2\mathbf{r}d\mathbf{r} \tag{16}$$

is the permanent dipole associated with $\phi_1(R,\mathbf{r})$. The above two-level model shows that for $\theta = 0^0$ with $\boldsymbol{\xi}(t)\cdot\mathbf{D}_p(R) \neq 0$, the asymmetric system initially in the $|0\rangle$ state will be coupled to the $|1\rangle$ state due to the effect of the permanent dipole. The situation is similar for the $|0\rangle$ state and a higher vibrational state such as $|2\rangle = \chi_1^{v=2}(R)\phi_1(R,r)$, resulting in the rapid motion of the nuclear wave packet associated with $\phi_1(R,r)$. Noting, for $\theta = 90^0$ with $\boldsymbol{\xi}(t)\cdot\mathbf{D}_p(R) \equiv 0$ and for symmetric molecules with $\mathbf{D}_p(R) \equiv 0$, these two vibrational states do not couple. In these cases, the motion of the nuclear wave packet of $\phi_1(R,r)$ is only related to the laser-induced excitation of the electronic states. This motion is usually far slower than the laser-permanent-dipole-induced one.

The amplitude $c_{\mathbf{p}}(R,t)$ of the rescattering wave packet is relevant to the vibrational wave function $\chi(R,\tau)$ [14], which obeys the Schrödinger equation of

$$i\frac{\partial\chi(R,\tau)}{\partial\tau} = \left[-\frac{1}{2\mu_N}\frac{\partial^2}{\partial R^2} + \frac{Z_{\mathrm{He}}Z_H}{R}\right]\chi(R,\tau) \tag{17}$$

with the initial condition $\chi(R,0) = \chi'(R,t_i)$. The function $\chi'(R,t_i)$ is the vibrational wave function of the continuum electron at the time t_i at which the continuum electron is born.

Let us discuss the amplitude $a_{\mathbf{p}(\omega)}(R)$ in more detail. First, for the parallel orientation, due to the effect of the permanent dipole, the bound wave packet $\psi_1(R,\mathbf{r},t)$ spreads towards larger R at which the ionization is usually easier to occur than at the equilibrium separation. This spreading is more remarkable for HeH^{2+} with lighter nuclei than HeT^{2+}. One can expect that the ionization yields of HeH^{2+} are also higher than HeT^{2+}. Accordingly, the amplitude $c_{\mathbf{p}}(R,t)$ of the rescattering wave packet, which is closely related to the ionization is also larger for HeH^{2+} than HeT^{2+}. This mechanism potentially increases the HHG yields of HeH^{2+} in comparison with HeT^{2+}. Second, due to the repulsion of these two nuclei, the rescattering wave packet $\psi_{\mathrm{re}}(R,\mathbf{r},t)$ also spreads rapidly towards larger R in the propagation process of HHG. This spreading is also more remarkable for HeH^{2+} with lighter nuclei than HeT^{2+}. This spreading reduces the overlap of these two amplitudes $a_1(R,t)$ and $c_{\mathbf{p}}(R,t)$ in recombination and therefore decreases the value of $a_{\mathbf{p}(\omega)}(R)$. This mechanism potentially reduces the HHG yields of HeH^{2+} in comparison with HeT^{2+}. One can expect that these two mechanisms compete in the HHG process. Due to this competition, the HHG yields of HeH^{2+} can be higher than HeT^{2+}. For the perpendicular orientation, the permanent dipole plays no role. This spreading of the bound wave packet $\psi_1(R,\mathbf{r},t)$ can be neglected. In this case, the spreading of the rescattering wave packet $\psi_{\mathrm{re}}(R,\mathbf{r},t)$ dominates in the HHG. As a result, the HHG yields of HeH^{2+} with lighter nuclei are usually lower than HeT^{2+}, as in the symmetric cases of H_2 versus T_2 [14]. In the following, we will perform a full analysis on the HHG process of the vibrating system to check the mechanisms discussed above.

III. RESULTS AND DISCUSSIONS

A. Comparisons between HHG spectra

Figure 1 plots the HHG spectra of HeH^{2+} versus HeT^{2+} at $\theta = 0^\circ$ (the left column) and $\theta = 90^\circ$ (right) for different laser intensities and wavelengths. For the case of low laser intensity of $I = 1.2\times10^{14}\mathrm{W/cm^2}$ with $\lambda = 1200$nm, one can observe that in Fig. 1(a) of $\theta = 0^\circ$, the HHG yields of HeH^{2+} with lighter nuclei are one order of magnitude higher than HeT^{2+}. However, in Fig. 1(d) of $\theta = 90^\circ$, this situation reverses and the HHG yields of HeT^{2+} become remarkably higher than HeH^{2+}. As we change the laser wavelength, the results with $\lambda = 1000$nm are similar to the cases of $\lambda = 1200$nm, as shown in Figs. 1(b) and 1(e). As we increase the laser intensity to $I = 4\times10^{14}\mathrm{W/cm^2}$, the HHG yields of HeH^{2+} become comparable with HeT^{2+} for $\theta = 0^\circ$, and are higher than HeT^{2+} in the high-energy region for $\theta = 90^\circ$, as shown in Figs. 1(c) and 1(f). The results in Fig. 1 imply that the HHG of the vibrating asymmetric system is closely related to the molecular orientation and the laser parameters.

A careful comparison between these results in Fig. 1 also shows that the HHG yields at the parallel orientation are usually several orders of magnitude higher than those at the perpendicular orientation, for both cases of HeH^{2+} and HeT^{2+}. Next, we explore the potential mechanism behind these phenomena.

B. Roles of nuclear motion in ionization

As the ionization is the first step of HHG, in Figs. 2(a) to 2(d), we compare the ionization yields of HeH^{2+} versus HeT^{2+} at $\theta = 0^\circ$ (the first column) and $\theta = 90^\circ$ (the second column) for different laser parameters. For the low laser intensity of $I = 1.2\times10^{14}\mathrm{W/cm^2}$, the ionization yields of HeH^{2+} are almost two orders of magnitude higher than HeT^{2+} at $\theta = 0^\circ$, as shown in Fig. 2(a). However, they are comparable at $\theta = 90^\circ$ (the HHG yields of HeH^{2+} are only two times higher than HeT^{2+}), as shown in Fig. 2(c). For the high laser intensity of $I = 4\times10^{14}\mathrm{W/cm^2}$, the ionization yields of HeH^{2+} and HeT^{2+} are comparable in both cases of $\theta = 0^\circ$ and $\theta = 90^\circ$, as shown in Figs. 2(b) and 2(d). In Figs. 2(e) and 2(f), we also show the comparison between the ionization yields of HeH^{2+} or HeT^{2+} at $\theta = 0^\circ$ versus $\theta = 90^\circ$. One can observe from Figs. 2(e) and 2(f) the ionization yields at $\theta = 0^\circ$ are almost four orders of magnitude higher than those at $\theta = 90^\circ$.

These results imply that for the parallel orientation, the ionization is remarkably stronger for lighter nuclei at relatively low laser intensities. In addition, the ionization yields differ significantly at $\theta = 0^\circ$ versus $\theta = 90^\circ$ for both cases of HeH^{2+} and HeT^{2+}. These results of ionization are in agreement with

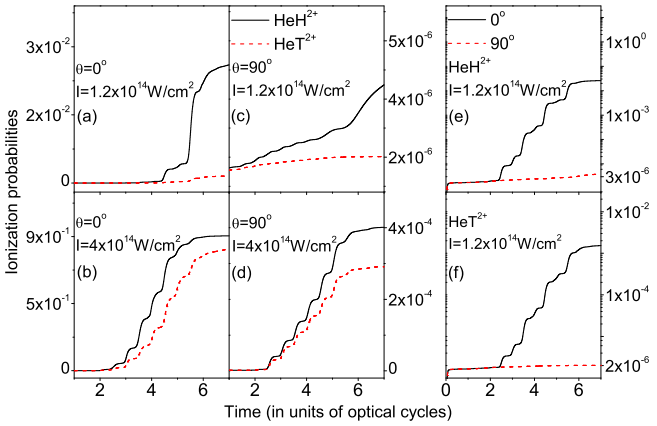

FIG. 2. Comparisons between ionization probabilities of HeH^{2+} (black solid) versus HeT^{2+} (red dashed) at $\theta = 0^\circ$ (the first column) and $\theta = 90^\circ$ (the second column), obtained with different laser intensities, as shown. For comparison, the result of HeT^{2+} in (a) is multiplied by a factor of 10. In the third column of Fig. 2, we also show the comparisons between ionization probabilities at $\theta = 0^\circ$ (black solid) vs $\theta = 90^\circ$ (red dashed) for HeH^{2+} (e) and HeT^{2+} (f), obtained with $I = 1.2 \times 10^{14}\mathrm{W/cm^2}$. The $\log_{10}$ scale is used in (e) and (f). The laser wavelength used is $\lambda = 1000$nm.

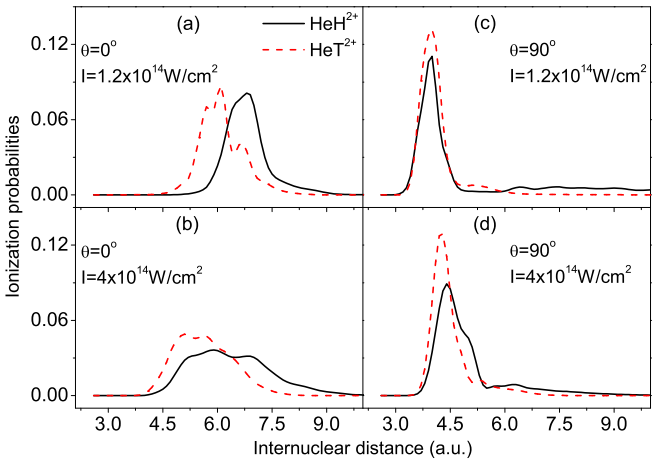

FIG. 3. Comparisons between R-dependent ionization probabilities $\Upsilon(R)$ of HeH^{2+} (black solid) versus HeT^{2+} (red dashed) at $\theta = 0^\circ$ (the left column) and $\theta = 90^\circ$ (right), obtained with different laser intensities, as shown. The laser wavelength used is $\lambda = 1000$nm.

the HHG results in Fig. 1, where the HHG yields of HeH^{2+} for the parallel case are also strikingly higher than HeT^{2+} at relatively low laser intensities, and the HHG yields of HeH^{2+} or HeT^{2+} also differ remarkably for the parallel orientation versus the perpendicular one. One therefore can expect that the ionization of the vibrating system plays an important role in the comparisons related to HHG in Fig. 1.

In the following, we analyze the influence of nuclear motion on the ionization. As discussed in Ref. [57], at $\theta = 0^\circ$, the interaction of the laser field and the permanent dipole of the asymmetric system induces the strong coupling between neighboring vibrational states. This coupling transfers the populations of the system from lower vibrational states to higher ones, resulting in the rapid spreading of the nuclear wave packet associated with the electronic BO bound state of the system. In other words, due to the effect of the permanent dipole, the asymmetric molecule tends to stretch to larger internuclear distances R at the parallel orientation. One can expect that this spreading of the nuclear wave packet is more remarkable for lighter nuclei. On the other hand, the molecule is also easier to ionize at larger R [19,23]. Consequently, the ionization yields of HeH^{2+} with lighter nuclei are higher than HeT^{2+}. One can expect that this mechanism, which increases the ionization yields, is more important for lower laser intensities at which the ionization is more difficult to occur near the equilibrium distance. At $\theta = 90^\circ$, the effect of the permanent dipole disappears and the spreading of the nuclear wave packet for HeH^{2+} and HeT^{2+} is similar. Accordingly, the ionization yields of HeH^{2+} and HeT^{2+} are also comparable.

To validate the above analyses, in Fig. 3, we plot R-dependent ionization probabilities $\Upsilon(R)$ averaged on the whole ionization probability, which are defined as

$$\Upsilon(R) = \frac{\int |\psi(R,\boldsymbol{r},t)|^2[1 - f(R,\boldsymbol{r})^2]d\boldsymbol{r}dt}{\int |\psi(R,\boldsymbol{r},t)|^2[1 - f(R,\boldsymbol{r})^2]dR d\boldsymbol{r}dt}, \qquad (18)$$

with $f(R,\boldsymbol{r}) = F(x)F(y)F(R)$. Here $F(x)$, $F(y)$, and $F(R)$ are the mask functions introduced in the part of numerical procedure. For the parallel orientation, the results in Fig. 3(a) of low laser intensity show that the ionization probability peaks at $R = 6.8$a.u. for HeH^{2+} and at $R = 6.1$a.u. for HeT^{2+}, implying that the HeH^{2+} molecule stretches to larger R than HeT^{2+}. For the case of high laser intensity in Fig. 3(b), the results show that the main contributions to ionization come from a broad range of R for both HeH^{2+} and HeT^{2+}. In addition, this range of R for large ionization probabilities is also broader for HeH^{2+} than HeT^{2+}. For the perpendicular orientation, however, the ionization for HeH^{2+} and HeT^{2+} predominately occurs at a similar R around [Fig. 3(c)] or somewhat larger than [Fig. 3(d)] the equilibrium separation. These results are in agreement with our above analyses in Fig. 2.

To further illuminate the permanent-dipole-induced remarkable enhancement of ionization for HeH^{2+} in comparison with HeT^{2+}, in Fig. 4 and Fig. 5, we plot the populations of some lower vibrational states $\chi_1^v(R)$ associated with the electronic 2σ BO state $\phi_1(R,\boldsymbol{r})$, and the populations of these two lower electronic BO states $\phi_1(R,\boldsymbol{r})$ versus $\phi_2(R,\boldsymbol{r})$ at $\theta = 0^\circ$. For comparison, the laser field $\xi(t)$ is also plotted here.

First, for HeH^{2+} in Fig. 4, one can observe from Fig. 4(c), the lowest vibrational state $\chi_1^\circ(R)$ also shows the rapid-asymmetric-depletion phenomenon, as for the case of HeH^+ in [57]. Specifically, the depletion of the state $\chi_1^\circ(R)$ is not symmetric in one laser cycle. In the first half cycle with $\xi(t) > 0$, this state depletes rapidly, when in the second half cycle with $\xi(t) < 0$, this state depletes slowly. This rapid-asymmetric-depletion phenomenon arises from the effect of the permanent dipole, which transfers the populations of the system from the $\chi_1^\circ(R)$ state to higher vibrational states $\chi_1^v(R)$,

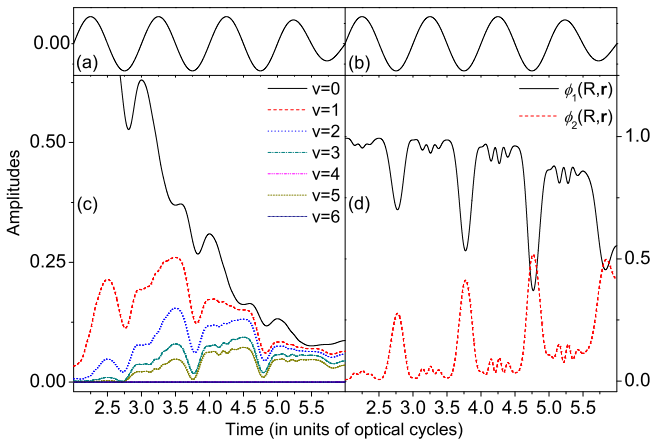

FIG. 4. (c) Time-dependent populations of the first vibrational states $\chi_1^{\upsilon}(R)$ of HeH^{2+} associated with the electronic BO first-excited state $\phi_1(R,\boldsymbol{r})$ and (d) time-dependent populations of these two lower electronic BO excited states $\phi_1(R,\boldsymbol{r})$ versus $\phi_2(R,\boldsymbol{r})$ of HeH^{2+}, obtained with $I = 1.2 \times 10^{14}\mathrm{W/cm^2}$, $\lambda = 1000\mathrm{nm}$ and $\theta = 0^\circ$. In (a) and (b), the laser field used here is also shown.

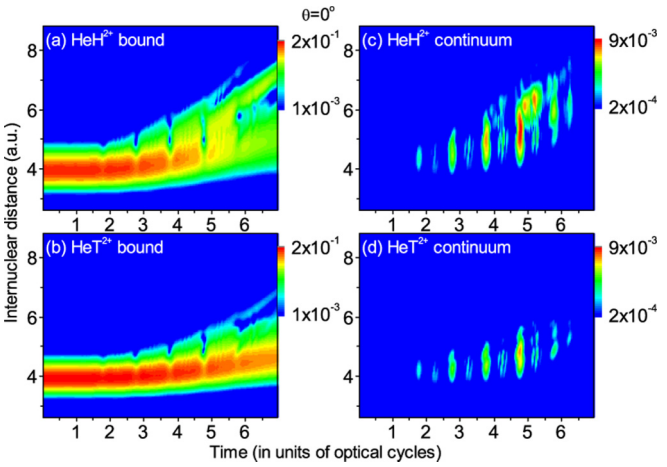

FIG. 6. R-time-dependent distributions $\eta(R,t)$ of bound wave packet $\psi_1(R,\mathbf{r},t)$ [(a), (b)] and $\alpha(R,t)$ of rescattering wave packet $\psi_{\mathrm{re}}(R,\mathbf{r},t)$ [(c), (d)] for HeH^{2+} (the first row) and HeT^{2+} (second), obtained with $I = 1.2 \times 10^{14}\mathrm{W/cm^2}$ and $\lambda = 1000$ nm at $\theta = 0^\circ$. The $\log_{10}$ scale is used here.

resulting in the rapid spreading of the nuclear wave packet associated with $\phi_1(R,\boldsymbol{r})$.

As the molecule stretches to larger R, the energy gap between these two lower electronic states $\phi_1(R,\boldsymbol{r})$ and $\phi_2(R,\boldsymbol{r})$ decreases. As a result, these two electronic states are more easily coupled together, as shown in Fig. 4(d). Here, one can observe the crossing of the populations of these two states, implying the transformation of the population from the initial electronic state $\phi_1(R,\boldsymbol{r})$ to the higher excited state $\phi_2(R,\boldsymbol{r})$. As the excited state $\phi_2(R,\boldsymbol{r})$ has a smaller ionization potential in comparison with that of $\phi_1(R,\boldsymbol{r})$, this population transformation also increases the ionization yields of the system.

The results for HeT^{2+} in Fig. 5 are somewhat similar to those in Fig. 4, but the depletion of the $\chi_1^{\circ}(R)$ state is slower in comparison with HeH^{2+} and the populations of these two electronic BO states $\phi_1(R,\boldsymbol{r})$ and $\phi_2(R,\boldsymbol{r})$ do not cross here. One can then expect that the spreading of the bound wave packet and the ionization yields for HeT^{2+} are smaller than HeH^{2+}. This phenomenon that the ionization yields of vibrating HeH^{2+} are higher than HeT^{2+} is somewhat similar to that introduced in Ref. [15] for H_2^+ versus D_2^+. The difference is that in the symmetric case, the effect of the permanent dipole is absent and the laser-induced motion of the nuclear wave packet associated with the bound electron is far slower than in the asymmetric case [57].

C. Roles of nuclear motion in rescattering

Previously, we have discussed the influence of nuclear motion on the ionization process. Next, we turn to the influence of nuclear motion on the propagation and the recombination processes of HHG. As discussed in Eq. (14), the HHG depends on the overlap of the bound wave packet $\psi_1(R,\boldsymbol{r},t)$ and the rescattering wave packet $\psi_{\mathrm{re}}(R,\boldsymbol{r},t)$. In Fig. 6 and Fig. 7, we plot the distributions of $\eta(R,t)$ associated with the bound wave packet and $\alpha(R,t)$ related to the rescattering one, which

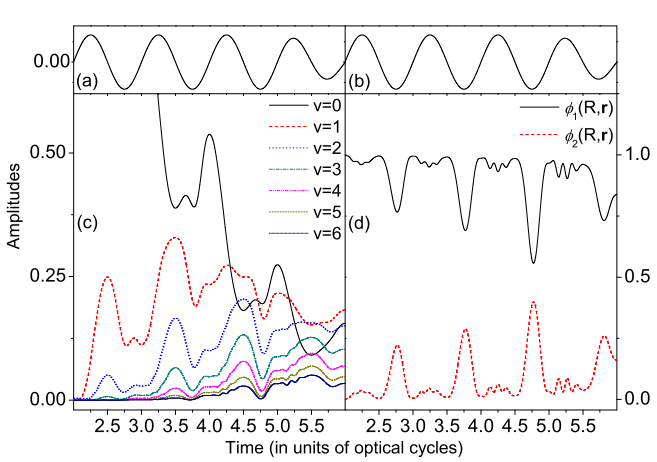

FIG. 5. Same as Fig. 4, but for HeT^{2+}.

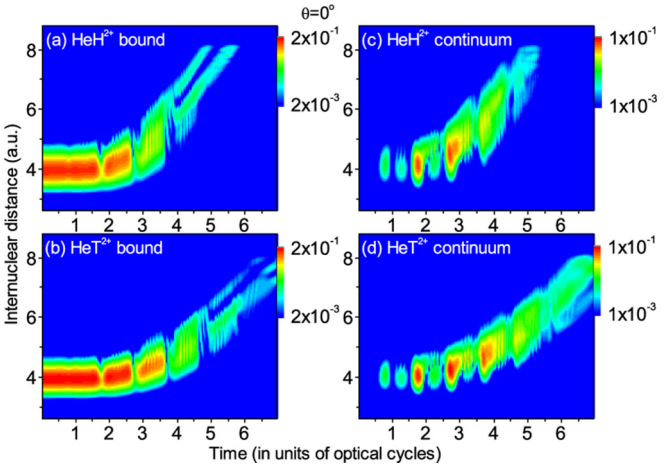

FIG. 7. Same as Fig. 6, but $I = 4 \times 10^{14}\mathrm{W/cm^2}$.

are defined as

$$\eta(R,t) = \int |\psi_1(R,\boldsymbol{r},t)|^2 d\boldsymbol{r};$$
$$\alpha(R,t) = \int |\psi_{\rm re}(R,\boldsymbol{r},t)|^2 d\boldsymbol{r}, \tag{19}$$

with $\psi_1(R,\boldsymbol{r},t) = a_1(R,t)\phi_1(R,\boldsymbol{r})$ and $a_1(R,t) = \langle\phi_1(R,\boldsymbol{r})|\psi_1(R,\boldsymbol{r},t)\rangle$. The definition of $\psi_{\rm re}(R,\boldsymbol{r},t)$ is as in Eq. (8).

Figure 6 plots the results obtained with $I = 1.2 \times 10^{14}$W/cm^2, $\lambda = 1000$nm, and $\theta = 0^\circ$. One can observe from Fig. 6(a), the bound distribution $\eta(R,t)$ for HeH^{2+} spreads to distances (near to 8 a.u.) much larger than the equilibrium separation (3.9 a.u.) as the time increases. The continuum distribution $\alpha(R,t)$ for HeH^{2+} in Fig. 6(c) behaves similarly to the bound one in Fig. 6(a), with spreading towards large R. By comparison, the distributions in Figs. 6(b) and 6(d) for HeT^{2+} spread to distances around $R = 6$a.u., smaller than HeH^{2+}. Considering that the HHG is dependent of the overlap of the bound and the rescattering wave packets in the recombination process, from these results in Fig. 6, one can expect that the HHG occurs at larger R for HeH^{2+} than HeT^{2+}. As the continuum distribution in Fig. 6(c) for HeH^{2+} has amplitudes remarkably larger than those in Fig. 6(d) for HeT^{2+}, the HHG yields of HeH^{2+} can be higher than those of HeT^{2+}, as observed in Fig. 1(b).

For $I = 4 \times 10^{14}$W/cm^2 and $\theta = 0^\circ$, all of the distributions in Fig. 7 for HeH^{2+} and HeT^{2+} spread towards large R (up to $R = 8$a.u.), and the corresponding distributions for HeH^{2+} and HeT^{2+} have similar amplitudes; one therefore can expect that the HHG yields of HeH^{2+} and HeT^{2+} are also similar in this case, as seen in Fig. 1(c). It is worth noting that in Fig. 7, the spreading of the distributions for HeH^{2+} is also quicker than HeT^{2+}. In particular, although all of the distributions in Fig. 7 span a wide range of R, they have large amplitudes at distances near to the equilibrium separation, implying that in this case the HHG of HeH^{2+} and HeT^{2+} mainly occurs near to the equilibrium geometry.

To provide an intuitive picture of the overlap of the distributions for HeH^{2+} and HeT^{2+}, which determines the HHG intensity, in Fig. 8, we compare R-dependent bound distributions $\zeta(R)$ versus continuum distributions $\beta(R)$, which are defined as

$$\zeta(R) = \frac{\int |\psi_1(R,\boldsymbol{r},t)|^2 d\boldsymbol{r}dt}{\int |\psi_1(R,\boldsymbol{r},t)|^2 dR d\boldsymbol{r}dt};$$
$$\beta(R) = \frac{\int |\psi_{\rm re}(R,\boldsymbol{r},t)|^2 d\boldsymbol{r}dt}{\int |\psi_{\rm re}(R,\boldsymbol{r},t)|^2 dR d\boldsymbol{r}dt}. \tag{20}$$

The overlap of the distributions $\zeta(R)$ and $\beta(R)$ is related to the part of the distributions where both of the bound and the rescattering wave packets have relatively large amplitudes. One can observe from each panel of Fig. 8, when the bound distribution $\zeta(R)$ shows a sharp peak near to the equilibrium separation, the continuum distribution $\beta(R)$ has large amplitudes at larger R. In addition, the bound and the continuum distributions show a striking crossing point, as indicated by the vertical arrows. One can expect that when the position of the crossing point is nearer to the equilibrium separation, the overlap of the distributions $\zeta(R)$ and $\beta(R)$ is also larger. The position of the crossing point therefore reflects the extent of overlap of these two distributions. We use this crossing point as a reference to approximately estimate the distance around which the HHG of the vibrating system mainly occurs. For the low-intensity cases, the position of the crossing point in Fig. 8(a) of HeH^{2+} is about 4.6 a.u. and it is 4.3 a.u. in Fig. 8(b) of HeT^{2+}. For the high-intensity cases, the position is 4.47 a.u. in Fig. 8(c) of HeH^{2+} and 4.38 a.u. in Fig. 8(d) of HeT^{2+}. The corresponding positions related to HeT^{2+} are somewhat smaller than HeH^{2+}, implying that the overlap for HeT^{2+} is larger than HeH^{2+}, in agreement with the argument that the spreading of both bound and rescattering wave packets for HeT^{2+} with heavier nuclei is slower than HeH^{2+}. These results in Fig. 8 show how, at the parallel orientation, the spreading of the bound and the rescattering wave packets influences the recombination process of HHG.

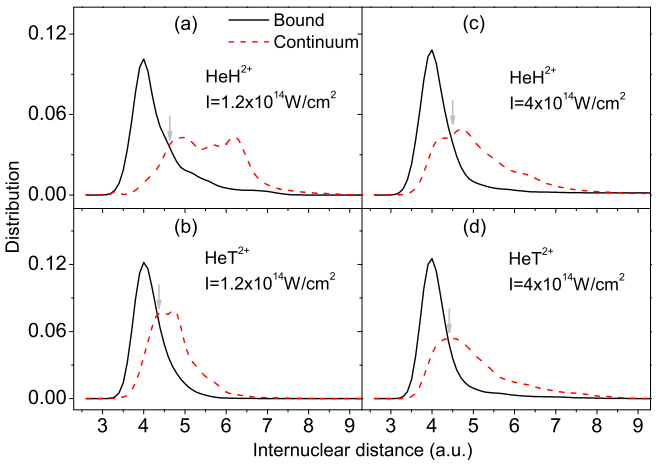

FIG. 8. Comparisons between probability distributions $\zeta(R)$ of bound wave packet $\psi_1(R,\boldsymbol{r},t)$ (black solid) versus $\beta(R)$ of rescattering wave packet $\psi_{\rm re}(R,\mathbf{r},t)$ (red dashed) for HeH^{2+} (the first row) and HeT^{2+} (second) at $\theta = 0^\circ$, obtained with different laser intensities, as shown. The laser wavelength used is $\lambda = 1000$nm.

For the perpendicular orientation, the situation is different, as shown in Fig. 9 and Fig. 10, where all of the distributions of $\eta(R,t)$ and $\alpha(R,t)$ have large amplitudes around the

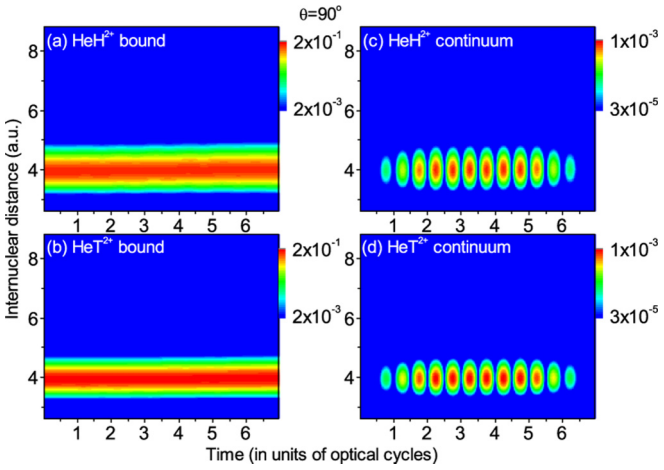

FIG. 9. Same as Fig. 6, but $\theta = 90^\circ$.

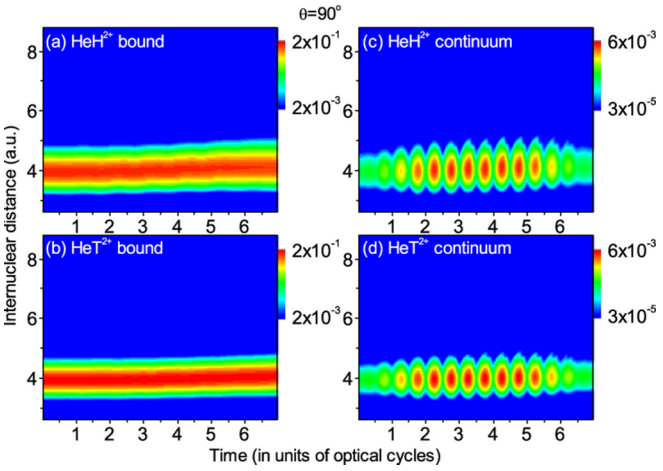

FIG. 10. Same as Fig. 7, but $\theta = 90^\circ$.

equilibrium separation (3.9 a.u.). These results imply that at $\theta = 90^\circ$, at which the permanent dipole of the system plays no role and accordingly the spreading of the bound wave packets is small, the dynamics of these two asymmetric molecules HeH^{2+} and HeT^{2+} are somewhat similar. The HHG of both of the two molecules mainly occurs around the equilibrium separation.

A careful comparison also shows that the spreading of the continuum distributions for HeH^{2+} in R space is somewhat broader than HeT^{2+} in Fig. 9 and Fig. 10. This broader spreading suppresses the recombination and therefore suppresses the HHG of HeH^{2+} in comparison with HeT^{2+}, as seen in Figs. 1(e) and 1(f). This suppression effect is usually stronger for high-energy harmonics associated with the rescattering electrons with longer excursion times in the laser field [14].

We mention that at the perpendicular orientation, the calculated distributions $\zeta(R)$ versus $\beta(R)$ for HeH^{2+} or HeT^{2+} basically coincide with each other with a sharp peak around the equilibrium separation, so we do not present them here.

IV. CONCLUSIONS

In summary, we have studied the HHG from the vibrating asymmetric molecule HeH^{2+} versus its isotopic variant HeT^{2+} with different molecular orientations and different laser parameters in strong few-cycle pulses. Our simulations showed that for the parallel orientation, the HHG yields of HeH^{2+} with lighter nuclei can be remarkably higher than those of HeT^{2+}. Our analyses reveal that the laser-induced vibrational motion of the bound wave packet plays an important role in this phenomenon. Specifically, due to the effect of the permanent dipole, the bound wave packet of the system associated with the initial electronic state tends to spread to larger internuclear distances R at which the asymmetric system is easier to ionize. For HeH^{2+} with lighter nuclei, the spreading of the bound wave packet is faster than HeT^{2+}. As a result, the ionization of HeH^{2+} is stronger than HeT^{2+}, especially for relatively low laser intensities at which the ionization near the equilibrium separation is difficult to achieve. This mechanism potentially increases the HHG yields of HeH^{2+}. On the other hand, the rescattering wave packet of HeH^{2+} associated with the rescattering electron also spreads more rapidly towards large R than HeT^{2+}. This spreading diminishes the overlap of the rescattering wave packet and the bound wave packet and therefore potentially reduces the HHG yields of HeH^{2+} in comparison with HeT^{2+}. These two mechanisms compete in the HHG process and this competition leads to the HHG yields of HeH^{2+} higher than HeT^{2+} at relatively low laser intensities. Our analyses based on a developed simple HHG model support this conclusion. We expect that the effect discussed in the paper for HeH^{2+} will also appear for other asymmetric molecules with a large permanent dipole.

ACKNOWLEDGMENTS

This work was supported by the National Natural Science Foundation of China (Grants No. 11274090 and No. 11404259), the Youth Foundation of Hebei Province Education Department (Grant No. QN2017028), and the Fundamental Research Funds for the Central Universities (Grant No. SNNU. GK201403002).

[1] P. B. Corkum and F. Krausz, Attosecond science, Nature Phys. **3**, 381 (2007).
[2] Z. Tao, C. Chen, T. Szilvasi, M. Keller, M. Mavrikakis, H. Kapteyn, and M. Murnane, Direct time-domain observation of attosecond final-state lifetimes in photoemission from solids, Science **353**, 62 (2016).
[3] F. Krausz and M. Ivanov, Attosecond physics, Rev. Mod. Phys. **81**, 163 (2009).
[4] P. Antoine, A. L'Huillier, and M. Lewenstein, Attosecond Pulse Trains Using High-Order Harmonics, Phys. Rev. Lett. **77**, 1234 (1996).
[5] Z. Chang, A. Rundquist, H. Wang, M. M. Murnane, and H. C. Kapteyn, Generation of Coherent Soft X Rays at 2.7 nm Using High Harmonics, Phys. Rev. Lett. **79**, 2967 (1997).
[6] M. Drescher, M. Hentschel, R. Kienberger, G. Tempea, C. Spielmann, G. A. Reider, P. B. Corkum, and F. Krausz, X-ray pulses approaching the attosecond frontier, Science **291**, 1923 (2001).
[7] J. Itatani, J. Levesque, D. Zeidler, H. Niikura, H. Pepin, J. C. Kieffer, P. B. Corkum, and D. M. Villeneuve, Tomographic imaging of molecular orbitals, Nature (Londun) **432**, 867 (2004).
[8] S. Haessler, J. Caillat, W. Boutu, C. Giovanetti-Teixeira, T. Ruchon, T. Auguste, Z. Diveki, P. Breger, A. Maquet, B. Carré, R. Taïeb, and P. Salières, Attosecond imaging of molecular electronic wavepackets, Nature Phys. **6**, 200 (2010).
[9] C. Vozzi, M. Negro, F. Calegari, G. Sansone, M. Nisoli, S. De Silvestri, and S. Stagira, Generalized molecular orbital tomography, Nature Phys. **7**, 822 (2011).
[10] Y. J. Chen, L. B. Fu, and J. Liu, Asymmetric Molecular Imaging through Decoding Odd-Even High-Order Harmonics, Phys. Rev. Lett. **111**, 073902 (2013).

[11] O. Smirnova, Y. Mairesse, S. Patchkovskii, N. Dudovich, D. Villeneuve, P. Corkum, and M. Yu. Ivanov, High harmonic interferometry of multi-electron dynamics in molecules, Nature (London) **460**, 972 (2009).

[12] D. Shafir, H. Soifer, B. D. Bruner, M. Dagan, Y. Mairesse, S. Patchkovskii, M. Yu. Ivanov, O. Smirnova, and N. Dudovich, Resolving the time when an electron exits a tunneling barrier, Nature (London) **485**, 343 (2012).

[13] P. M. Kraus, B. Mignolet, D. Baykusheva, A. Rupenyan, L. Horný, E. F. Penka, G. Grassi, O. I. Tolstikhin, J. Schneider, F. Jensen, L. B. Madsen, A. D. Bandrauk, F. Remacle, and H. J. Wörner, Measurement and laser control of attosecond charge migration in ionized iodoacetylene, Science **350**, 790 (2015).

[14] M. Lein, Attosecond Probing of Vibrational Dynamics with High-Harmonic Generation, Phys. Rev. Lett. **94**, 053004 (2005).

[15] X. B. Bian and A. D. Bandrauk, Probing Nuclear Motion by Frequency Modulation of Molecular High-Order Harmonic Generation, Phys. Rev. Lett. **113**, 193901 (2014).

[16] H. J. Wörner, J. B. Bertrand, D. V. Kartashov, P. B. Corkum, and D. M. Villeneuve, Following a chemical reaction using high-harmonic interferometry, Nature (London) **466**, 604 (2010).

[17] P. B. Corkum, Plasma Perspective on Strong Field Multiphoton Ionization, Phys. Rev. Lett. **71**, 1994 (1993).

[18] M. Lewenstein, Ph. Balcou, M. Yu. Ivanov, A. L'Huillier, and P. B. Corkum, Theory of high-harmonic generation by low-frequency laser fields, Phys. Rev. A **49**, 2117 (1994).

[19] T. Zuo and A. D. Bandrauk, Charge-resonance-enhanced ionization of diatomic molecular ions by intense lasers, Phys. Rev. A **52**, R2511(R) (1995).

[20] Y. J. Chen, J. Chen, and J. Liu, Charge-resonance effect on harmonic generation by symmetric diatomic molecular ions in intense laser fields, Phys. Rev. A **74**, 063405 (2006).

[21] W. Becker, J. Chen, S. G. Chen, and D. B. Milošević, Dressed-state strong-field approximation for laser-induced molecular ionization, Phys. Rev. A **76**, 033403 (2007).

[22] J. Chen and S. G. Chen, Gauge problem in molecular high-order harmonic generation, Phys. Rev. A **75**, 041402(R) (2007).

[23] Y. J. Chen and B. Zhang, Strong-field approximations for the orientation dependence of the total ionization of homonuclear diatomic molecules with different internuclear distances, J. Phys. B **45**, 215601 (2012).

[24] R. Velotta, N. Hay, M. B. Mason, M. Castillejo, and J. P. Marangos, High-Order Harmonic Generation in Aligned Molecules, Phys. Rev. Lett. **87**, 183901 (2001).

[25] H. Stapelfeldt and T. Seideman, Aligning molecules with strong laser pulses, Rev. Mod. Phys. **75**, 543 (2003).

[26] X. X. Zhou, X. M. Tong, Z. X. Zhao, and C. D. Lin, Alignment dependence of high-order harmonic generation from N_2 and O_2 molecules in intense laser fields, Phys. Rev. A **72**, 033412 (2005).

[27] M. Lein, N. Hay, R. Velotta, J. P. Marangos, and P. L. Knight, Role of the Intramolecular Phase in High-Harmonic Generation, Phys. Rev. Lett. **88**, 183903 (2002).

[28] T. Kanai, S. Minemoto, and H. Sakai, Quantum interference during high-order harmonic generation from aligned molecules, Nature (London) **435**, 470 (2005).

[29] C. Vozzi, F. Calegari, E. Benedetti, J.-P. Caumes, G. Sansone, S. Stagira, M. Nisoli, R. Torres, E. Heesel, N. Kajumba, J. P. Marangos, C. Altucci, and R. Velotta, Controlling Two-Center Interference in Molecular High Harmonic Generation, Phys. Rev. Lett. **95**, 153902 (2005).

[30] Y. J. Chen, J. Liu, and Bambi Hu, Intensity dependence of intramolecular interference from a full quantum analysis of high-order harmonic generation, Phys. Rev. A **79**, 033405 (2009).

[31] J. Levesque, Y. Mairesse, N. Dudovich, H. Pepin, J.-C. Kieffer, P. B. Corkum, and D. M. Villeneuve, Polarization State of High-Order Harmonic Emission from Aligned Molecules, Phys. Rev. Lett. **99**, 243001 (2007).

[32] X. Zhou, R. Lock, N. Wagner, W. Li, H. C. Kapteyn, and M. M. Murnane, Elliptically Polarized High-Order Harmonic Emission from Molecules in Linearly Polarized Laser Fields, Phys. Rev. Lett. **102**, 073902 (2009).

[33] S.-K. Son, D. A. Telnov, and S.-I. Chu, Probing the origin of elliptical high-order harmonic generation from aligned molecules in linearly polarized laser fields, Phys. Rev. A **82**, 043829 (2010).

[34] S. Ramakrishna, P. A. J. Sherratt, A. D. Dutoi, and T. Seideman, Origin and implication of ellipticity in high-order harmonic generation from aligned molecules, Phys. Rev. A **81**, 021802(R) (2010).

[35] P. A. J. Sherratt, S. Ramakrishna, and T. Seideman, Signatures of the molecular potential in the ellipticity of high-order harmonics from aligned molecules, Phys. Rev. A **83**, 053425 (2011).

[36] S. Yu, B. Zhang, Y. Li, S. Yang, and Y. Chen, Ellipticity of odd-even harmonics from oriented asymmetric molecules in strong linearly polarized laser fields, Phys. Rev. A **90**, 053844 (2014).

[37] C. D. Liu, Z. N. Zeng, P. F. Wei, P. Liu, R. X. Li, and Z. Z. Xu, Driving-laser wavelength dependence of high-order harmonic generation in H_2^+ molecules, Phys. Rev. A **81**, 033426 (2010).

[38] Jian Wu, H. Zeng, and Chunlei Guo, Triple-ionization-induced dissociation of NO in strong laser fields, Phys. Rev. A **74**, 031404(R) (2006).

[39] A. Rupenyan, P. M. Kraus, J. Schneider, and H. J. Wörner, Quantum interference and multielectron effects in high-harmonic spectra of polar molecules, Phys. Rev. A **87**, 031401(R) (2013); High-harmonic spectroscopy of isoelectronic molecules: Wavelength scaling of electronic-structure and multielectron effects, **87**, 033409 (2013).

[40] H. Akagi, T. Otobe, A. Staudte, A. Shiner, F. Turner, R. Dörner, D. M. Villeneuve, and P. B. Corkum, Laser tunnel ionization from multiple orbitals in HCl, Science **325**, 1364 (2009).

[41] G. L. Kamta and A. D. Bandrauk, Phase Dependence of Enhanced Ionization in Asymmetric Molecules, Phys. Rev. Lett. **94**, 203003 (2005).

[42] X. B. Bian and A. D. Bandrauk, Multichannel Molecular High-Order Harmonic Generation from Asymmetric Diatomic Molecules, Phys. Rev. Lett. **105**, 093903 (2010).

[43] Y. Chen and B. Zhang, Role of excited states in the emission times of harmonics from asymmetric molecules, Phys. Rev. A **86**, 023415 (2012).

[44] X. Y. Miao and H. N. Du, Theoretical study of high-order-harmonic generation from asymmetric diatomic molecules, Phys. Rev. A **87**, 053403 (2013).

[45] R. F. Lu, C. Yu, Y. H. Wang, Q. Shi, and Y. D. Zhang, Control of electron localization to isolate and enhance molecular harmonic plateau in asymmetric HeH^{2+} system, Phys. Lett. A **378**, 90 (2014).

[46] J. Heslar, D. Telnov, and S.-I. Chu, High-order-harmonic generation in homonuclear and heteronuclear diatomic molecules: Exploration of multiple orbital contributions, Phys. Rev. A **83**, 043414 (2011).

[47] A. Etches and L. B. Madsen, Extending the strong-field approximation of high-order harmonic generation to polar molecules: gating mechanisms and extension of the harmonic cutoff, J. Phys. B **43**, 155602 (2010).

[48] B. B. Augstein and C. Figueira de Morisson Faria, Multielectron corrections in molecular high-order harmonic generation for different formulations of the strong-field approximation, J. Mod. Opt. **58**, 1173 (2011).

[49] X. Zhu, Q. Zhang, W. Hong, P. Lan, and P. Lu, Two-center interference in high-order harmonic generation from heteronuclear diatomic molecules, Opt. Express **19**, 436 (2011).

[50] H. Du, L. Luo, X. Wang, and B. Hu, Generating isolated elliptically polarized attosecond pulses from oriented CO gas medium using linearly polarized driving pulses, Phys. Rev. A **86**, 013846 (2012).

[51] E. Frumker, C. T. Hebeisen, N. Kajumba, J. B. Bertrand, H. J. Wörner, M. Spanner, D. M. Villeneuve, A. Naumov, and P. B. Corkum, Oriented Rotational Wave-Packet Dynamics Studies via High Harmonic Generation, Phys. Rev. Lett. **109**, 113901 (2012).

[52] E. Frumker, N. Kajumba, J. B. Bertrand, H. J. Wörner, C. T. Hebeisen, P. Hockett, M. Spanner, S. Patchkovskii, G. G. Paulus, D. M. Villeneuve, A. Naumov, and P. B. Corkum, Probing Polar Molecules with High Harmonic Spectroscopy, Phys. Rev. Lett. **109**, 233904 (2012).

[53] Y. Pan, S.-F. Zhao, and X.-X. Zhou, Generation of isolated sub-40-as pulses from gas-phase CO molecules using an intense few-cycle chirped laser and a unipolar pulse, Phys. Rev. A **87**, 035805 (2013).

[54] P. M. Kraus, D. Baykusheva, and H. J. Wörner, Two-Pulse Field-Free Orientation Reveals Anisotropy of Molecular Shape Resonance, Phys. Rev. Lett. **113**, 023001 (2014).

[55] P. M. Kraus, A. Rupenyan, and H. J. Wörner, High-Harmonic Spectroscopy of Oriented OCS Molecules: Emission of Even and Odd Harmonics, Phys. Rev. Lett. **109**, 233903 (2012).

[56] X. Y. Miao and C. P. Zhang, Multichannel recombination in high-order-harmonic generation from asymmetric molecular ions, Phys. Rev. A **89**, 033410 (2014).

[57] W. Y. Li, S. J. Yu, S. Wang, and Y. J. Chen, Probing nuclear dynamics of oriented HeH+ with odd-even high-order harmonics, Phys. Rev. A **94**, 053407 (2016).

[58] J. R. Hiskes, Dissociation of molecular ions by electric and magnetic fields, Phys. Rev. **122**, 1207 (1961).

[59] M. D. Feit, J. A. Fleck, Jr., and A. Steiger, Solution of the Schrödinger equation by a spectral method, J. Comput. Phys. **47**, 412 (1982).

[60] X. M. Tong, S. Watahiki, K. Hino, and N. Toshima, Numerical Observation of the Rescattering Wave Packet in Laser-Atom Interactions, Phys. Rev. Lett. **99**, 093001 (2007).